Hollow core–shell $Co_9S_8@ZnIn_2S_4/CdS$ nanoreactor for efficient photothermal effect and CO_2 photoreduction

Yan Zhang [a], Yixiao Wu [a], Liang Wan [a], Huijun Ding [b], Huixiang Li [a], Xiyang Wang [c], Weihao Zhang [a,*]

[a] College of Resource and Environmental Science, Hubei Biomass-Resource Chemistry and Environmental Biotechnology Key Laboratory, Wuhan University, Wuhan 430072, PR China
[b] Jiangxi Provincial Key Laboratory of Water Resources and Environment of Poyang Lake, Jiangxi Institute of Water Sciences, Nanchang, Jiangxi 330029, PR China
[c] State Key Laboratory of Inorganic Synthesis and Preparative Chemistry, Jilin Provincial International Cooperation Key Laboratory of Advanced Inorganic Solid Functional Materials, College of Chemistry Jilin University, Changchun 130012, PR China

ABSTRACT

The hollow core–shell Co_9S_8 @$ZnIn_2S_4$/CdS nanoreactors are fabricated by growing $ZnIn_2S_4$ nanosheets and CdS quantum dots on hollow Co_9S_8 nanocages for photocatalytic CO_2 reduction and H_2 generation. Because of unique structural and compositional advantages, Co_9S_8 @$ZnIn_2S_4$/CdS exhibits a significant photocatalytic BPA degradation of 90.62%, CO production of 82.10 µmol g^{-1} h^{-1}, and H_2 evolution rate up to 1419.14 µmol g^{-1} h^{-1}. Excellent photocatalytic performances are attributed to unique core-shell architecture, which can improve the scattering and refraction efficiency of incident light, and the separation and migration of photoinduced carriers. Furthermore, Co_9S_8 @$ZnIn_2S_4$/CdS possesses a broad absorption spectrum facilitating outstanding photothermal performance. The photocatalytic mechanism for the nanoreactor has been discussed in detail.

1. Introduction

Bisphenol A (BPA) is as the industrial compound, mainly used in the field of fine chemicals [1]. The illegal emission of industrial effluent and its mishandling leading to the widespread presence of BPA in aquatic environment [2]. Besides, BPA as a typical endocrine disruptor has attracted wide public concern that causes serious effects of human health. So it is necessary to explore an efficient technology to eliminate BPA from water. Photocatalysis is able to effectively remove BPA with the utilization of solar energy. Moreover, the photocatalytic reduction of CO_2 into useful hydrocarbons is an effective approach for solving the energy crunch and global warming [3]. The sustained consumption of non-renewable energy has caused an energy crisis, so converting CO_2 into CH_4, CO, CH_3OH, and other compounds by photocatalysis is effectual in solving these issues [4]. However, the photoreduction of CO_2 suffers from low efficiency and utilization of sunlight [5–7] because CO_2 is a linear molecule with relatively high thermodynamic stability owing to higher bond energy of C═O (750 kJ mol^{-1}) in comparison to the bond energies of C–C (336 kJ mol^{-1}), C–O (327 kJ mol^{-1}), and C–H (411 kJ mol^{-1}). The photocatalytic conversion of CO_2 can break C═O bonds [8]

and hence, solar energy is suitable for this conversion. However, it requires photocatalysts with suitable band structure, which can be excited by solar light. Therefore, developing novel photocatalysts to improve CO_2 reduction with high efficiency is essential. To widen the utilization of the solar spectrum, infrared photocatalysis is required. UV–Vis can excite charges and Vis–IR increase the surface temperature of the photocatalyst to realize photothermal effect. Therefore, the limitation of low solar energy utilization in photocatalysis is circumvented. The significance of photothermal effect is that the synergistic effect of light and heat, which accelerates the charge transfer, and promotes the photocatalytic reaction.

Hollow structured materials have been investigated for solar energy conversion because they display prominent advantages. In particular, they can provide abundant active sites to accelerate the photocatalytic process and initiate reflection and scattering effect leading to enhanced light-absorption capability [9]. In addition, thin shells in these materials can also reduce the distance for rapid transfer of photogenerated charge to accelerate the reaction process [10]. To prepare hollow nanostructures, various synthesis methods have been developed including the conventional hard-templating approach. Nonetheless, this process

---

* Corresponding author.
E-mail address: weihao.zhang@outlook.com (W. Zhang).

requires a uniform coating around the surface and heat treatment to remove the template, which is complex and arduous. Most of the precursors utilized to fabricate hollow structures are still limited to unstable metal salts or hydroxides, in addition, the prepared materials are limited to metal or metal oxides. Hence, preparing high-quality hollow nanostructures with complex compositions and morphology is challenging.

Recently, core-shell nanostructures have caused wide concern because of unique morphology and application in various fields. In particular, core-shell photocatalysts provide the driving force for degradation reactions. They also possess active sites at the core or embedded within the void to improve stability. Therefore, the synthesis of hollow core–shell structure can enhance the separation of photogenerated carriers and photostability, consequently ameliorating the photocatalytic performance. The design of hollow core–shell nanoreactor has attracted wide attention, it is an ideal framework in a nanochamber and can be used for storage, sensing, and confinement effects in catalytic processes [11]. The hollow core–shell nanoreactor possess advantages, such as large enclosed void room and high surface-to-volume ratio [12]. The nanoreactor as a vital material, the shell structure can enable mass transfer for the reactive species while maintaining the stability of the core-shell framework. The void space between the shell and the cores provides unique functionality and working place for confined photocatalysis reaction.

Metal-organic (MOFs) frameworks consist of metal centers with organic linkers and comprise various structures and morphologies [13]. Hollow nanostructures can be produced using the MOFs as templates. In this study, the ZIF-67 precursors are used as templates to obtain hollow Co_9S_8 morphology. Co_9S_8 possess a narrow band gap and displays efficient charge transport via intermediate sulfur atoms bonded to other metals at the interface, demonstrating excellent photocatalytic activity. However, Co_9S_8 has few limitations including intrinsic poor electrical conductivity and instability, which hinders its practical applications [14,15]. The fabrication of a heterojunction is an effective method to avoid these limitations. The coupling of the semiconductors will generate a built-in electric field in the space charge region and thus accelerate the separation and migration of photoinduced charges [16]. Moreover, photocatalysts possessing heterostructures achieve better optical harvesting and photostability [17]. Consequently, combining Co_9S_8 with other semiconductor materials is effective for enhancing the photocatalytic performance.

The growth of two-dimensional semiconductor nanosheets on the Co_9S_8 cages is promising in reducing diffusion length of ions and improving the photocatalytic active sites. $ZnIn_2S_4$ has gained popularity as a ternary chalcogenide semiconductor material, owing to low toxicity, suitable band structure, special electronic, optical properties, and significantly high photocatalytic stability [18–20]. Hence, preparing novel photocatalysts composed of this material for CO_2 photoreduction is desirable.

CdS quantum dots (QDs) are metal chalcogenide, which have excellent properties [21], such as good crystallinity, excellent dispersity, and short bulk-to-surface diffusion distance for e^- and h^+ pairs [22]. The short diffusion distance is beneficial for fast migration of the photogenerated charges. Furthermore, QDs with size of 2–10 nm have outstanding properties, such as adjustable size, unique electron characteristics, and quantum confined effect. These properties help the material to display excellent photocatalytic hydrogen generation activity [23]. Therefore, growing QDs on Co_9S_8 @$ZnIn_2S_4$ hollow structures will facilitate the shortening of transmission distance of the photoinduced charges and expose more active sites. Consequently, the effective approach to synthesize the hollow core-shell Co_9S_8 @$ZnIn_2S_4$/CdS heterojunction is crucial.

The preparation of hierarchical Co_9S_8/$ZnIn_2S_4$ tubular type-I heterostructure by growing $ZnIn_2S_4$ nanosheets on the surface of hollow Co_9S_8 nanotubes. The unique hierarchical hollow tubular structure provides rich reaction sites in the photocatalytic process, which is conducive to separating and transferring of photoinduced e^- and h^+.

Thus, the hollow hierarchical heterostructure Co_9S_8/$ZnIn_2S_4$ exhibit an excellent H_2 evolution rate [24]. In addition, the type II hierarchical Co_9S_8 @$ZnIn_2S_4$ heterojunction for H_2 production is constructed. The unique structure efficiently contributes to the separation and transport of photoinduced charges for photocatalytic activities. The Co_9S_8 @$ZnIn_2S_4$ hollow heterojunction shows remarkable H_2 production rate and high stability due to the distinctive structural and compositional benefits [38]. Owing to inverse interfacial transfer of photoinduced e^- and h^+ pairs, the Co_9S_8 @$ZnIn_2S_4$ binary heterojunctions no matter type II or Z-scheme heterojunction can improve photocatalytic performance. But some of the reduction and oxidation potential of carriers are wasted during their transfer towards lower conduction band (CB) and higher valence band (VB). To solve this disadvantage, it is necessary to add a third component CdS in the heterojunction to enhance the CB potential. The improvement of the photocatalytic reaction in the ternary systems is ascribed to the synergistic effect of multicomponent that facilitates the migration and separation of charges and provides carriers with excellent oxidation and reduction potential. Moreover, compare with the binary heterostructure, the appropriate bandgap position in Co_9S_8 @$ZnIn_2S_4$/CdS ternary heterostructure enhances light absorption and enables efficient separation of photoinduced charges.

In this work, we develop rational design to prepare a novel hollow core–shell Co_9S_8 @$ZnIn_2S_4$/CdS heterostructure via solvothermal sulfidation reaction, oil bath and chemical deposition methods. The unique design of the hollow core-shell nanoreactor provides abundant active sites in the photocatalytic process. In addition, this method can ensure full contact of vis–NIR-active Co_9S_8, $ZnIn_2S_4$, and CdS, which contributes to separating and transporting photoexcited carriers. Therefore, the enhanced photoactivity results from the synergetic effect between heterojunction and the hollow structure. The hollow core-shell Co_9S_8 @$ZnIn_2S_4$/CdS nanoreactor provides outstanding CO_2 reduction and H_2 generation performances. The energy band and internal electric field of the nanoreactor are illustrated by simulated calculations. This study may provide novel methods to increase the photocatalytic activity and further understand the photocatalytic mechanism.

2. Experimental section

2.1. Preparation of ZIF-67

2.9 g of $Co(NO_3)_2$.6 H_2O was dispersed in 100 mL of methanol. Subsequently, the resultant solution was added into 100 mL of methanol containing 6.5 g of 2-methylimidazole. After complete mixing, the solution was aged at 20 °C for one day. The aged solution was centrifuged, and washed thrice with methanol. Therefore, the purple precipitates were obtained by dried in vacuum at 60 °C overnight.

2.2. Preparation of hollow Co_9S_8

To prepare hollow Co_9S_8, 80 mg of ZIF-67 and 0.12 g of thioacetamide (TAA) were added in 40 mL of ethanol. The mixture was then put into a Teflon-lined stainless-steel autoclave. The solvothermal reaction was carried out at 120 °C for 4 h. The hollow Co_9S_8 was washed with ethanol several times and denoted as CoS.

2.3. Preparation of hollow core-shell Co_9S_8 @$ZnIn_2S_4$

To grow the $ZnIn_2S_4$ nanosheets on the surface of the hollow Co_9S_8 dodecahedra, 8 mL of glycerol was dissolved in 32 mL of H_2O (pH = 2.5), subsequently, 100 mg of Co_9S_8 was added and stirred for 30 min, and then 272 mg of $ZnCl_2$, 586 mg of $InCl_3$.4 H_2O, and 300 mg of TAA were added. The resulting mixture was stirred for 15 min and then transferred into oil bath and stirred for 2 h at 80 °C. The final products were washed thrice with ethanol and dried at 60 °C in vacuum and denoted as CoS@ZIS.
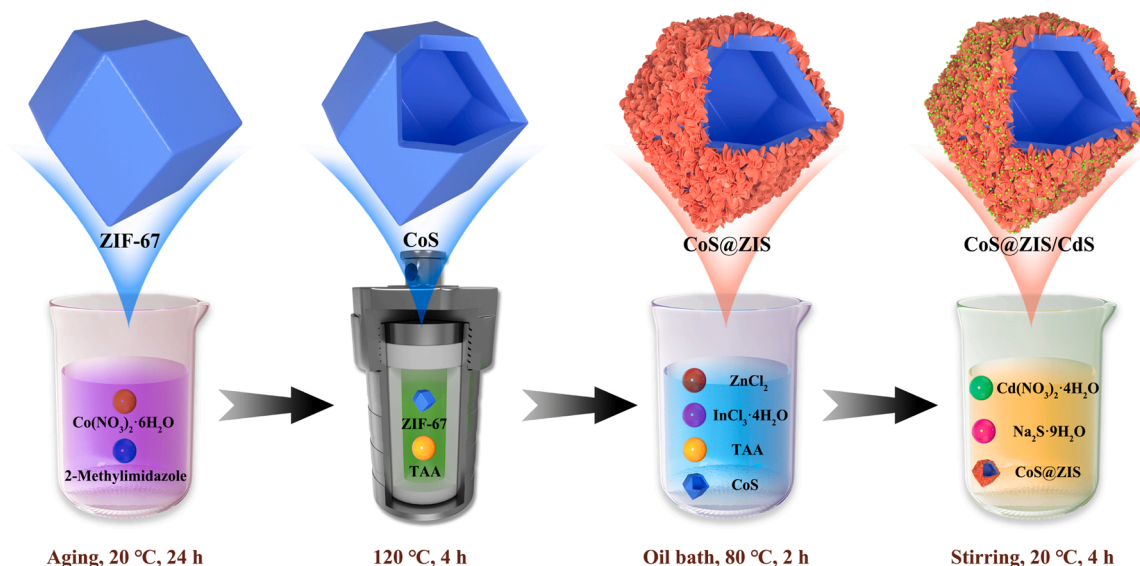
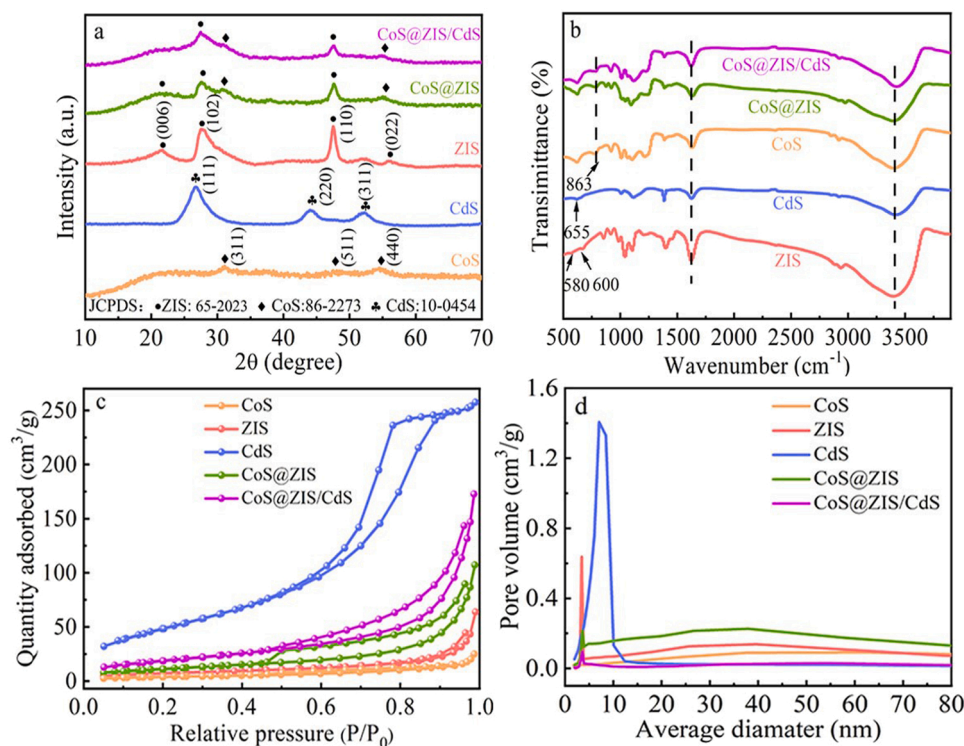**Fig. 1.** Schematic of the preparation of CoS@ZIS/CdS nanoreactor.

Fig. 2. XRD patterns (a), Raman spectras (b), N_2 adsorption–desorption isotherm curves (c), and pore size distribution curves (d) of CoS, ZIS, CdS, CoS@ZIS and CoS@ZIS/CdS.

2.4. Preparation of hollow core-shell Co_9S_8 @$ZnIn_2S_4$/CdS

To prepare hollow core-shell Co_9S_8 @$ZnIn_2S_4$/CdS, 0.1 g of Co_9S_8 @$ZnIn_2S_4$ was dispersed in 2 mmol $Cd(NO_3)_2$.4 H_2O with 100 mL anhydrous ethanol, then, 0.2 mmol $Na_2S·9 H_2O$ was introduced, and the solution was magnetic stirred at 20 °C for 4 h. Therefore, after washing several times and drying at 60 °C for 12 h, the Co_9S_8 @$ZnIn_2S_4$/CdS hollow heterojunction was prepared and denoted as CoS@ZIS/CdS. CdS was prepared with the same method without the addition of CoS@ZIS. The preparation of CoS@ZIS/CdS nanoreactor is exhibited in Fig. 1.

3. Results and discussion

3.1. Structural and morphological characterization

The crystal structure and phase composition of different photo-catalysts are investigated by X-ray diffraction (XRD) analysis. XRD pattern confirms the formation of ZIF-67 (Fig. S1). The diffraction peaks at 29.88°, 47.68°, and 52.18° shown in Fig. 2(a) can be indexed to the (311), (511), and (440) planes of cubic CoS phase (PDF No. 86–2273) [25], respectively. Moreover, the characteristic peaks at 21.68°, 27.78°, 47.28°, 52.48°, and 55.68°, corresponding to (006), (102), (110), (116),
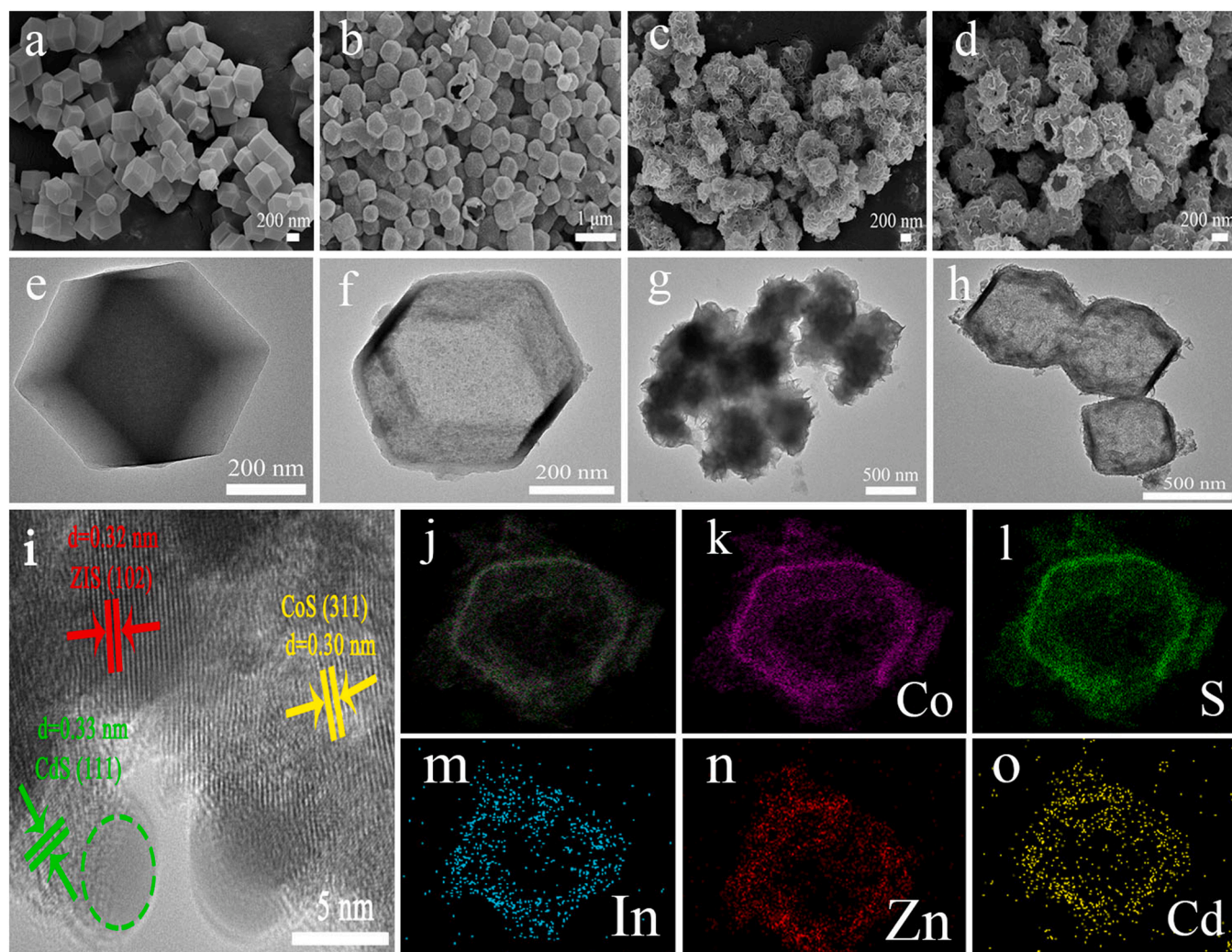
Fig. 3. SEM (a–d) and TEM (e–h) images of the prepared ZIF-67, CoS, ZIS, and CoS@ZIS/CdS composite, HRTEM image (i) of CoS@ZIS/CdS, and EDX elemental mapping images (j–o) of Co, S, Zn, In, and Cd of the CoS@ZIS/CdS composite.

and (022) planes [26], respectively, match well with the hexagonal $ZnIn_2S_4$ (JCPDS No. 65–2023). Furthermore, the prominent peaks observed at 26.6°, 43.8° and 51.8° are attributed to the (111), (220) and (311) planes of the cubic phase CdS (JCPDS #10–0454) [27]. In addition, the (331) and (440) planes belong to CoS, the (102) and (110) planes ascribed to the hexagonal ZIS, the CoS@ZIS and CoS@ZIS/CdS comprise the characteristic peaks of both CoS and ZIS, however, the characteristic peaks of CoS@ZIS/CdS obviously decrease. CdS can not be observed because of the low content of CdS. Raman spectra is used to verify the existence of CdS in the CoS@ZIS/CdS heterojunction (Fig. 2 (b)). The Raman peaks located at 183 cm^{-1}, 505 cm^{-1}, 599 cm^{-1} and 665 cm^{-1} belongs to CoS [28]. The diffraction peaks are observed at 300 cm^{-1}, and 600 cm^{-1} [29], corresponding to the stretching modes of ZIS and CoS@ZIS. The peaks are observed at 300 cm^{-1}, 601 cm^{-1} and 902 cm^{-1} [30] ascribed to CdS. The CoS@ZIS/CdS also shows the same peaks of CdS at 300 cm^{-1} and 601 cm^{-1}, however, the peaks obviously decrease, indicating the three components in the heterojunction.

Furthermore, the large specific surface area improves the photocatalytic activity, generating more active sites and efficient transport paths. The results of nitrogen adsorption–desorption experiments are exhibited in Fig. 2(c), five composites have type IV isotherm with H3 type hysteresis loop, indicating mesopores exist in the samples. The BET surface areas of the samples are also estimated, and the CoS@ZIS composite shows a higher BET surface area (41.56 m^2/g) than pure CoS (14.57 m^2/g), this suggests that the ZIS nanosheets can significantly improve the BET surface area of CoS@ZIS providing more active sites for photocatalysis. The surface areas, pore sizes, and pore volumes are listed in Table S2. BET surface areas of the CoS@ZIS/CdS are enhanced due to the addition of CdS, which are beneficial for adsorption of the reactant and further improving the photocatalytic reactions. Pore size distribution curves show the presence of mesopores in CoS@ZIS/CdS composite (Fig. 2(d)), which is conducive to separating charges during photocatalysis.

The morphologies and microstructures of photocatalysts are observed by scanning electron microscopy (SEM) and transmission electron microscopy (TEM). Different reaction times for preparing CoS have been showed in Fig. S5, indicating that 4 h is the most appropriate for the synthesis of CoS. The SEM and TEM images shown in Fig. 3(a) and (e) suggest that ZIF-67 has a polyhedra structure and smooth surface with uniform size of approximately 600 nm. During the sulfidation process, S^{2-} ions released from TAA upon hydrolyzation quickly react with Co^{2+} ions on the surface of ZIF-67 and generate a thin layer of sulfides. The ionic radius of Co^{2+} ion (74 pm) is smaller than the ionic radius of S^{2-} ion (184 pm), therefore, the outward diffusion of Co^{2+} ions is easier than the inward diffusion of S^{2-} ions [31]. Finally, the Co^{2+} ions released from ZIF-67 diffuse into the preformed cobalt sulfide layer and react with S^{2-} ions, which leading to the formation of the hollow structure. In Fig. 3(b) and (f), SEM and TEM images show that the morphology of CoS comprises open gap and cavity. As displayed in Fig. 3 (c) and (g), the SEM and TEM images show the nanosheets structure of
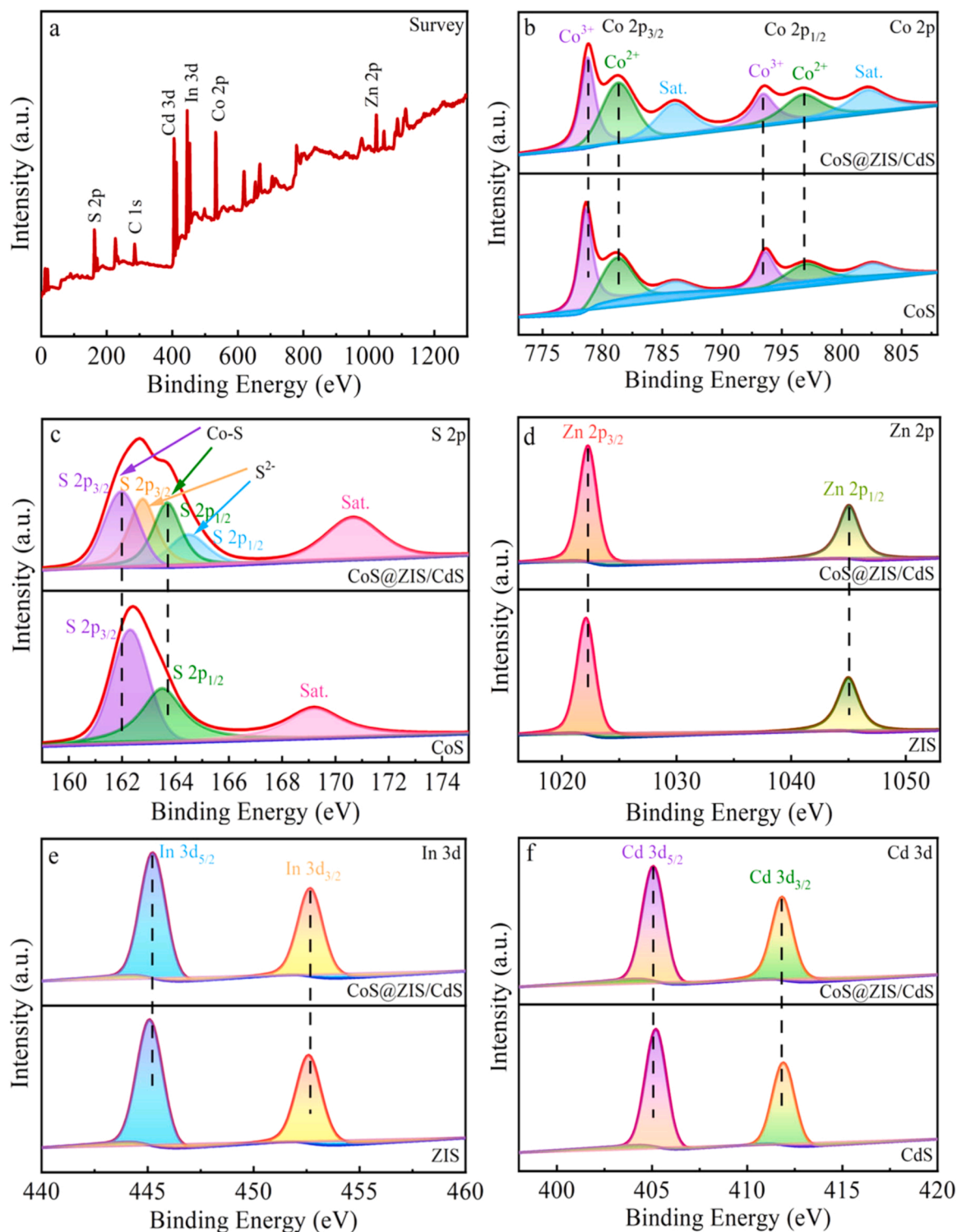
Fig. 4. XPS spectra of CoS@ZIS/CdS (a) survey spectrum, XPS comparison of Co 2p (b) and S 2p (c) in the CoS@ZIS/CdS and pristine CoS, XPS comparison of Zn 2p (d) and In 3d (e) in the CoS@ZIS/CdS and pristine ZIS, and XPS comparison of Cd 3d (f) in the CoS@ZIS/CdS and pristine CdS.

ZIS. The SEM images of CoS@ZIS/CdS composite is shown in Fig. 3(d). From the images it can be inferred that, the entire surface of the CoS hollow polyhedra with open ends is uniformly covered with ZIS nanosheets, leading to a rough surface. The size of CdS QDs are small and cannot be observed on the surface of CoS@ZIS. Moreover, the TEM images shown in Fig. 3(h) also validate the hollow structure of the CoS@ZIS/CdS composite. The HRTEM image in Fig. 3(i) exhibits the lattice fringe of 0.30 nm assigned to the (311) crystal plane of CoS [32].

The ZIS nanosheets with an interlayer spacing of 0.32 nm are identified as the (102) crystal plane of hexagonal ZIS [33]. The clear lattice fringe of 0.33 nm are ascribed to the (111) plane of CdS [34]. Furthermore, the elemental mapping images in Figs. 3(j)–(o) and S2 confirm that the coexistence of Co, S, In, Zn, and Cd elements in the hollow CoS@-ZIS/CdS heterojunction, indicating the uniform distribution in CoS@ZIS/CdS.
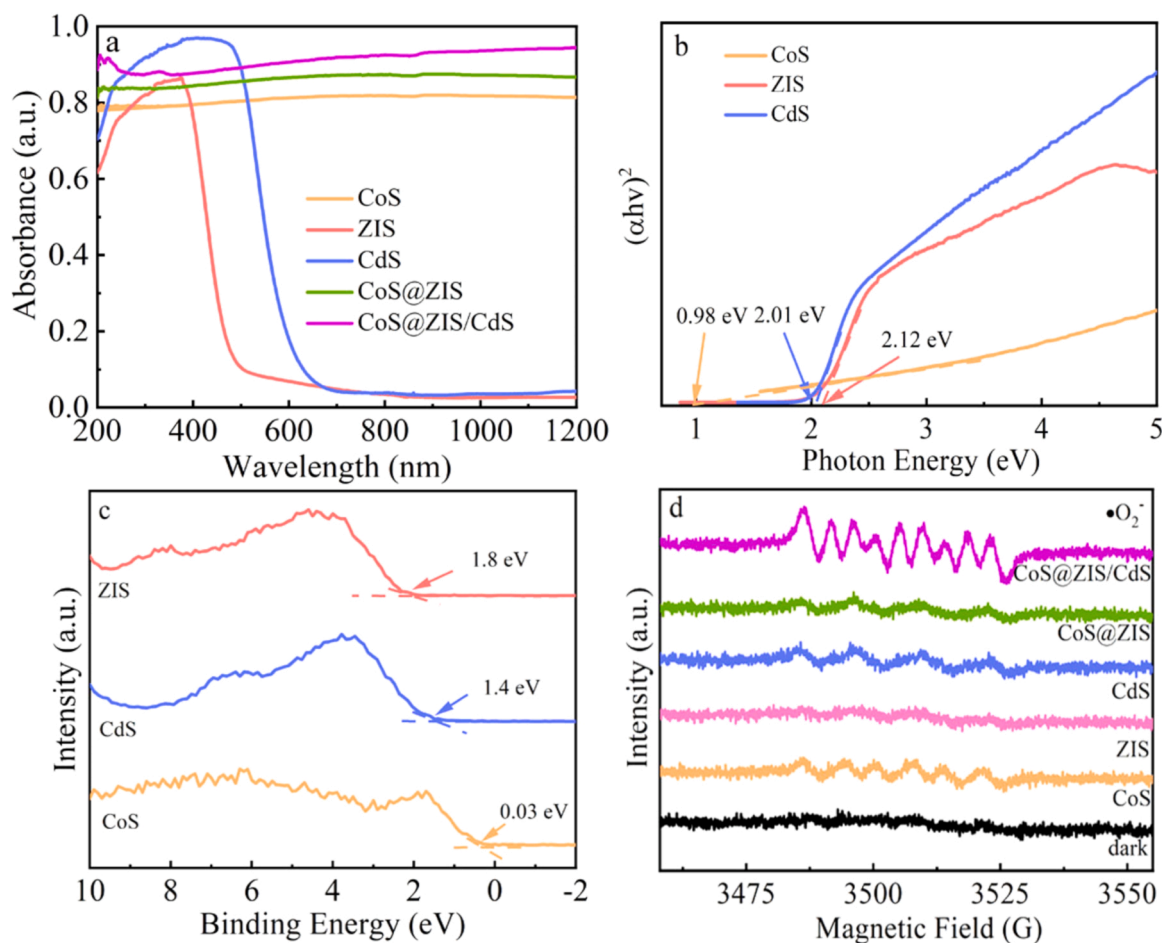
Fig. 5. Vis–NIR absorption spectra (a), band gap energies (b), XPS VB spectra (c) of CoS, ZIS, CdS samples, ESR of DMPO-trapped·O_2^- (d) in methanol using of CoS, ZIS, CdS, CoS@ZIS, and CoS@ZIS/CdS with visible-light irradiation.

3.2. Determination of interfacial charge transfer

Theoretical calculation is used to verify the enhanced electrical conductivity. The cell models used in the density functional theory (DFT) calculations are shown in Fig. S6. A semiconductor with suitable band structure is required for the fabrication of heterojunction. In Fig. S7(a), (c), and (e), the band structure is calculated by DFT and the estimated band gap of the CoS, ZIS and CdS are approximately 3.23, 2.32 and 1.67 eV, respectively. This indicates that the theoretical bandgap values of ZIS and CdS are close to the experimental values, however, the bandgap of CoS is not close to the experimental value, which is ascribed to the inherent lack of derivative discontinuity and delocalization error [35]. The calculated density of states (DOS) of CoS, ZIS, and CdS are shown in Fig. S7(b), (d), and (f), the Co p, S p, Zn p, In d, and Cd d orbitals are involved in electronic hybridization. The increase in the degree of hybridization facilitates the electron transfer in the photocatalytic reaction. This consequently increases the photocatalytic activity of CoS@ZIS/CdS. The formation of heterojunction among CoS, ZIS and CdS are important for highly efficient and stable. DFT calculations have provided deep insight into understanding the transport pathway of photogenerated charges across the interface and obtaining the nature of the photocatalytic reaction.

Mott-Schottky plots are collected to determine the types of semiconductors and flat-band potentials. ZIS, CoS, and CdS are all n-type semiconductors owing to negative slopes. In Fig. S8(b), (d), and (f), the flat-band potentials (V_{fb}) of CoS, ZIS and CdS are approximately −0.95, −0.35 and −0.36 eV vs. Ag/AgCl, respectively. Therefore, the V_{fb} of CoS, ZIS, and CdS are estimated to be −0.75, −0.15, and −0.16 eV vs.

normal hydrogen electrode (NHE), respectively. For n-type semiconductors, fermi level (E_f) is approximately equal to V_{fb} [36], therefore, CoS has a lower E_f than the E_f of CdS and ZIS. In Fig. S8(a), (c), and (e), the average potential profiles of CoS, ZIS, and CdS are calculated by DFT. According to the equation:

$$\Phi = E_{vac} - E_f \qquad (1)$$

where, E_{vac} represents vacuum energy level, E_f represents fermi level, and work function of CdS and ZIS are estimated to be 3.89 and 5.50 eV, respectively, which are smaller than that of the CoS (6.73 eV). The results suggest strong coupling interactions among three materials. The materials avoid charge consumption at the electron mediator and promote efficient separation of photoinduced $e^-–h^+$ pairs, thus achieving excellent redox property, leading to the increased photocatalytic performances of the heterostructure.

3.3. Analysis of electronic properties

The elemental composition and valence states of the CoS@ZIS/CdS composite are studied by X-ray photoelectron spectroscopy (XPS). The Co, S, Zn, In, and Cd elements are detected in the survey spectrum of CoS@ZIS/CdS (Fig. 4(a)). As exhibited in Fig. 4(b), two spin-orbit doublets and two satellite peaks (Sat.) are shown in the Co 2p spectrum. The characteristic peaks at 778.6 and 781.2 eV and those at 793.6 and 797.1 eV are corresponding to Co $2p_{3/2}$ and Co $2p_{1/2}$, respectively. The doublets indicate the coexistence of Co^{2+} and Co^{3+}, which are consistent with the Co valence state of CoS. Compared with pure CoS, the binding energies of Co 2p shift from 778.2 and 793.9 eV in CoS to
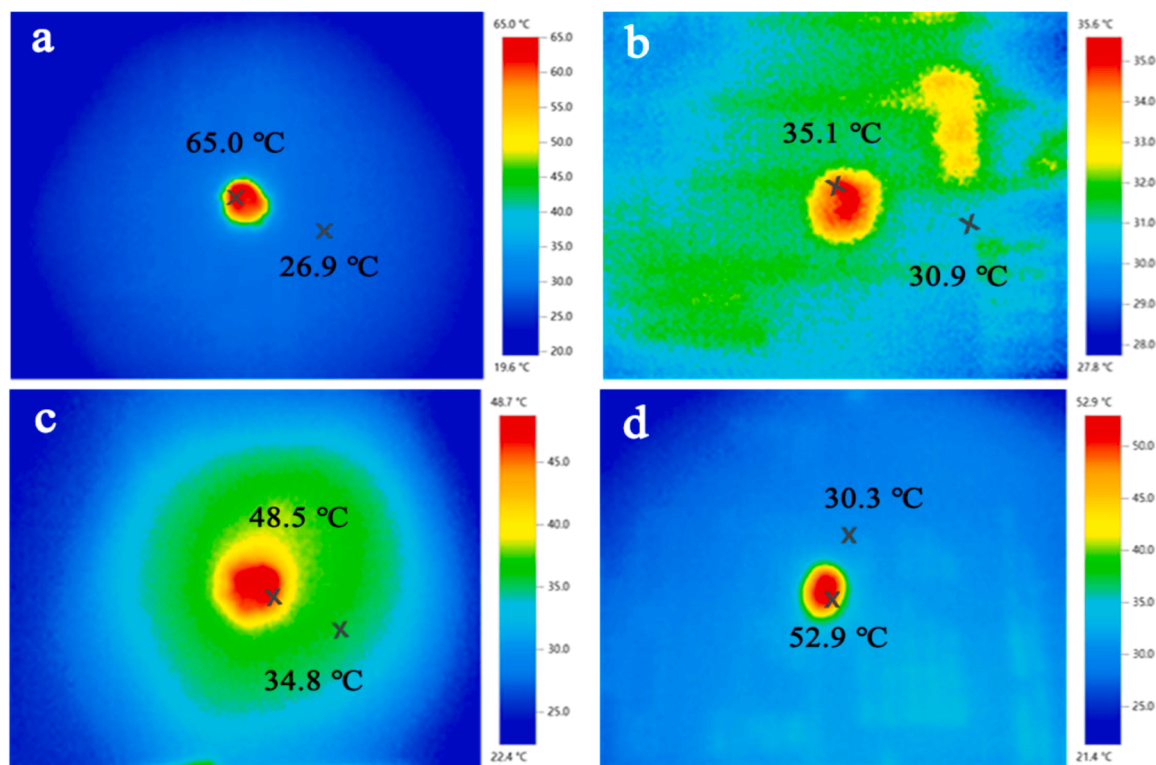
Fig. 6. IR images of CoS (a), ZIS (b), CdS (c), and CoS@ZIS/CdS (d) with irradiation time of 60 s.

778.6 and 793.6 eV in the CoS@ZIS/CdS heterojunction, indicating a strong interaction among CoS, ZIS and CdS [37]. In the S 2p spectrum (Fig. 4(c)), three S 2p peaks at 163.1 and 161.6, 168.9 eV are ascribed to the S $2p_{1/2}$ and S $2p_{3/2}$ orbitals of Co-S bonds and a shakeup satellite, respectively, corresponding to the results of previous reports on CoS [38]. In contrast, the two peaks at 163.8 and 162.3 eV are attributed to the S $2p_{1/2}$ and S $2p_{3/2}$ orbitals of S^{2-} ions in CoS@ZIS/CdS, which are consistent with the ZIS and CdS. As displayed in Fig. 4(d), the peaks with binding energies of 1045 and 1022.1 eV are assigned to Zn $2p_{1/2}$ and Zn $2p_{3/2}$, respectively [39]. Furthermore, in Fig. 4(e), two peaks at 445.1 and 452.6 eV correspond to In $3d_{5/2}$ and In $3d_{3/2}$, suggesting the chemical state of In^{3+} in the composite [40]. In Fig. 4(f), the Cd 3d spectrum shows characteristic peaks at 411.9 and 405.2 eV derived from Cd $3d_{3/2}$ and $3d_{5/2}$, which correspond to Cd^{2+} of CdS [41]. The shift in binding energies in Zn, In and Cd of CoS@ZIS/CdS compared to pure ZIS and CdS are observed. The positive shift of binding energy means decreased electron density, while the negative shift represents increased electron density. Compare with the binding energies of the ZIS, the peaks of Zn 2p and In 3d in CoS@ZIS/CdS shift towards the higher binding energy. However, the peaks position of Cd 3d and Co 2p shift to lower binding energies. These shifts indicate that the change of electron density around the atoms and a strong electronic interaction [42] with the electron transfer from ZIS to CoS and CdS in the CoS@ZIS/CdS heterojunction, which is beneficial for the construction of Z-scheme heterojunction.

3.4. Photothermal effect

Vis–NIR absorption spectroscopy is used to study the optical absorption of the photocatalysts. As shown in Fig. 5(a), CoS exhibits a high and wide absorption in the range of UV, visible and infrared regions, indicating excellent photothermal effect. Evidently, CoS/ZIS and CoS@ZIS/CdS shows high absorption in the infrared range because of their narrow band gap and unique hollow structure. As observed in Fig. 5(b), the bandgaps of CoS, ZIS and CdS are approximately 0.98 [43],

2.12 [44], and 2.01 eV [45], respectively. In addition, to further understand the photocatalytic mechanism of the CoS@ZIS/CdS composite, the measured valence band (VB) values of CoS, ZIS, and CdS are positioned at 0.03, 1.80 and 1.40 eV, respectively (Fig. 5c). The conduction band (CB) values of CoS, ZIS, and CdS are calculated as −0.95, −0.32, and −0.60 eV, respectively. Furthermore, ESR measurement is used to study the Z-scheme mechanism and analyze the location of e^- and h^+ pairs. As shown in Fig. 5(d), no signal of DMPO $\cdot\cdot O_2^-$ can be observed in dark, indicating that no valid e^- or h^+ were generated under dark conditions. The strongest characteristic signal of DMPO $\cdot\cdot O_2^-$ are observed in CoS@ZIS/CdS under visible-light irradiation of 3 min, since the CB position of CoS is higher than the $O_2/\cdot O_2^-$ (−0.33 V vs. NHE), promoting the e^- in the CB of CoS reduces O_2 to $\cdot O_2^-$. Since $\cdot O_2^-$ is produced from the separated photoexcited e^-, the improvement of $\cdot O_2^-$ proves that CoS@ZIS/CdS has stronger ability to separate photoinduced $e^- – h^+$ pairs, thus enhancing the photocatalytic degradation of BPA. In Fig. S9, no characteristic peaks of DMPO $\cdot\cdot OH$ are generated in CoS@-ZIS/CdS with visible-light irradiation, because the VB position of CdS and ZIS are more less than the oxidation potential of $H_2O/\cdot OH$ (2.34 V vs. NHE). Therefore, Z-scheme structure is affirmed.

The change of surface temperature of photocatalysts is investigated by the infrared (IR) camera. In Fig. 6(b) and (c), the temperature of bare ZIS and CdS are 35.1 °C and 48.5 °C after 60 s of solar light irradiation. The core temperature of the CoS increases from 26.9 °C to 65 °C in 60 s with simulated sunlight irradiation, as shown in Fig. 6(a), and the core temperature of the CoS@ZIS and CoS@ZIS/CdS rapidly increases to 65 °C (Fig. S10) and 52.9 °C in 60 s (Fig. 6(d)). After the addition of CoS, both CoS@ZIS and CoS@ZIS/CdS possess excellent solar-thermal conversion efficiency. A higher photocatalyst surface temperature can increase the rate of adsorption, diffusion, reaction, electron transport, and enhance the thermal activation [46]. The result suggests that photocatalysts initiate the photothermal effect owing to the strong light absorption in the from ultraviolet to infrared light range. In Fig. S11, the color of CoS and CoS@ZIS/CdS are black, in general, black materials often possess excellent photothermal effect, corresponding to the results
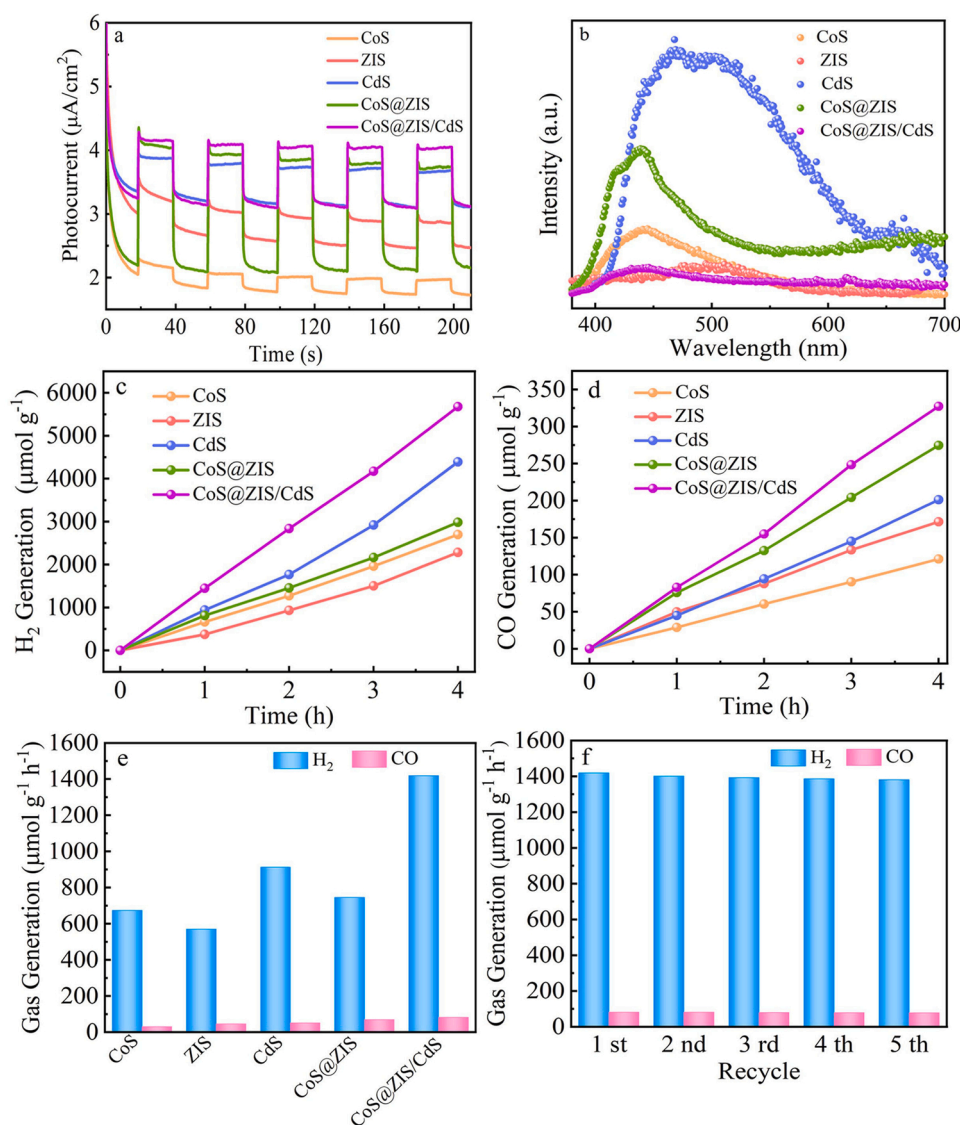
Fig. 7. Photocurrent responses (a), steady-state PL spectra of the as-prepared photocatalysts (b). Photocatalytic H_2 (c) and CO (d) output changes with light irradiation duration. Comparison of H_2 and CO generation over different samples (e). Cycling experiments of photocatalytic H_2 and CO generation over CoS@ZIS/CdS heterojunction (f).

observed from infrared images [47]. Therefore, the solar-thermal conversion of CoS@ZIS/CdS promotes the transport of charges, CoS@-ZIS/CdS possesses a high solar-thermal conversion property.

3.5. Photoelectrochemical and photocatalytic performances

Photoelectrochemical tests are conducted to investigate the separation and recombination of photogenerated charges of the photocatalysts. In Fig. 7(a), CoS, ZIS and CoS@ZIS show very low photocurrent densities. Following the CdS loading on the surface of the CoS@ZIS composite, CoS@ZIS/CdS shows the highest photocurrent density at approximately 4.3 µA/cm². This confirms that the CoS@ZIS/CdS composite possesses excellent interfacial separation efficiency of e⁻–h⁺ pairs. Moreover, the electrochemical impedance spectroscopy plots (EIS) provide further evidence. In Fig. S12, EIS measurements show that the CoS@ZIS/CdS composite has a smaller semicircle than the sole counterparts, confirming faster e⁻ transfer in the composites, which can be ascribed to the better conductivity of CoS. These results of photoelectrochemical tests demonstrate the increased separation and transfer of photoexcited carriers in CoS@ZIS/CdS, leading to the outstanding photocatalytic property of H_2 generation and CO_2 reduction.

PL spectrum is used to verify the charge separation efficiency. Low intensity of PL peak indicates the low recombination rate of photoexcited charges. In Fig. 7(b), CdS shows the strongest PL peak, after introducing CoS, the fluorescence of CoS@ZIS is efficiently quenched, indicating the addition of CoS inhibits the recombination of photogenerated e⁻ and h⁺ pairs [48]. The CoS@ZIS/CdS heterojunction exhibits the lowest intensity of PL, showing the superior charge separation and migration ability.

The photocatalytic performance of the samples is evaluated by degrading BPA with visible-light irradiation. After 120 min photocatalytic reaction, the removal rate at 5 mg/L reaches up to 95.45%, which is 21.27% higher than that at 20 mg/L (Fig. S13), the removal rate at 10 mg/L is 90.62%. Considering the concentration of BPA exists in water environment, 10 mg/L is the best choice. Besides, the influence of photocatalyst-dosage experiments are carried out. Series dosages of CoS@ZIS/CdS are investigated when the initial concentration of BPA is maintained at 10 mg/L. The removal rates of 25 mg, 50 mg, 75 mg, and 100 mg reach up to 77.35%, 90.62%, 93.15% and 99.92% (Fig. S14). The results indicate that the larger amount of photocatalysts, the higher removal rate of BPA can be obtained. The influences of different pH values ranging from 2 to 10 are also investigated. It is found that
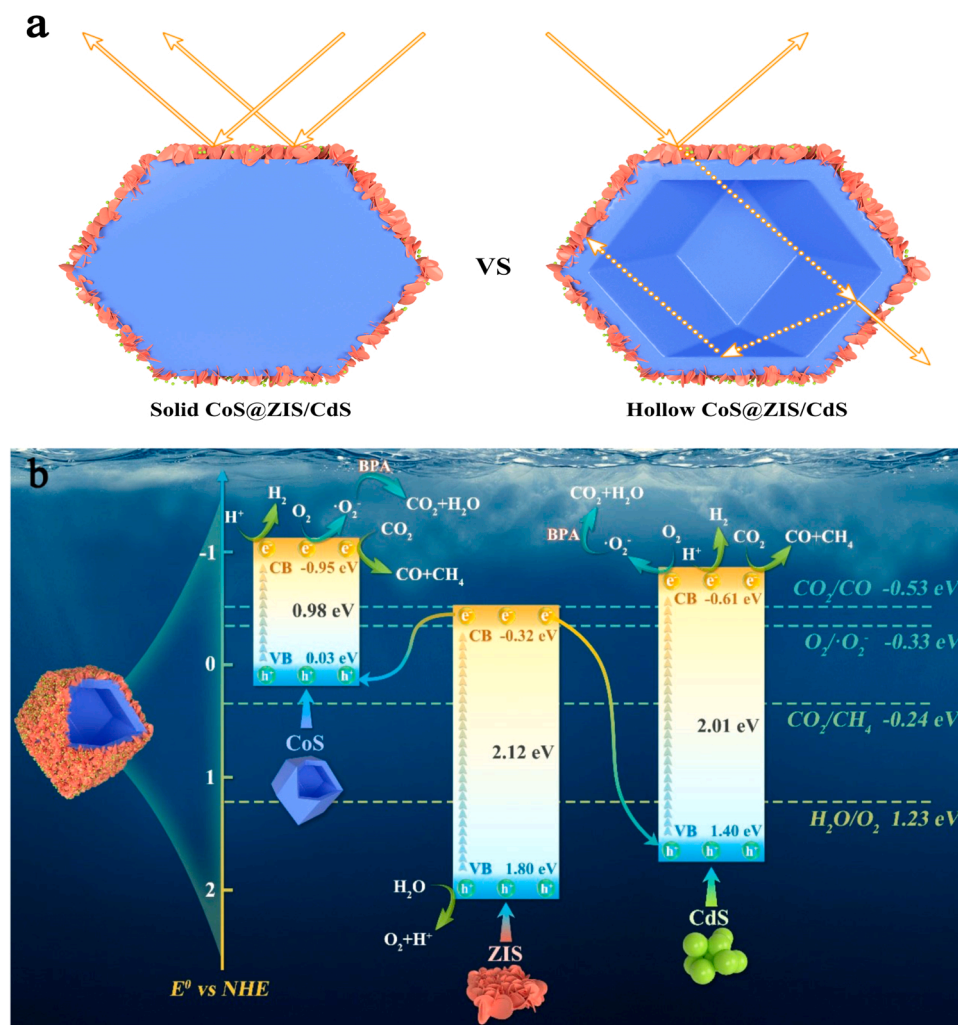
Fig. 8. Illustration of multiple reflections (a) and proposed photocatalytic mechanism over CoS@ZIS/CdS heterojunction (b).

CoS@ZIS/CdS exhibits good performances toward BPA degradation and there is only 4.0% difference between pH = 2 and pH = 10. Especially, BPA degradation efficiency achieves 90.74% at pH = 4 (Fig. S15), suggesting that photocatalytic BPA degradation prefers to be carried out with acidic conditions. In Fig. S16, without photocatalysts, the concentration of BPA is stable, implying that the photocatalysts play a key role in the photocatalytic degradation of BPA. Furthermore, the reduction efficiency of BPA for CoS@ZIS/CdS composite reaches 90.62%, which is higher than the reduction efficiencies of pure CoS, ZIS and CdS. This enhanced photocatalytic activity is because CoS@ZIS/CdS has unique hollow core-shell heterostructure and effectively promotes the interfacial separation and transport of photoinduced charges.

The photocatalytic performances of as-prepared photocatalysts are also assessed by H_2 and CO generation. Fig. 7(c) and (d) summarize the H_2 and CO generation amount of pure CoS, ZIS, CdS, CoS@ZIS, and CoS@ZIS/CdS composite within 4 h. The amount of H_2 and CO produce from photocatalysts steadily increases over time. In Fig. 7(e), pure CoS and ZIS display poor photocatalytic activity for H_2 and CO generation, probably resulting from the high recombination of photoinduced carriers. The yields of H_2 obtained on these photocatalysts are in the order of ZIS < CoS < CoS@ZIS < CdS < CoS@ZIS/CdS. Surprisingly, the H_2 generation of CoS@ZIS/CdS is highest (1419.14 μmol g^{-1} h^{-1}) among the reported CoS-based, ZIS-based and CdS-based materials, as shown in Table S3. The yields of CO increase in the order of CoS < ZIS < CdS < CoS@ZIS < CoS@ZIS/CdS. CoS@ZIS/CdS also shows the highest CO production rate of 82.10 μmol g^{-1} h^{-1}, which is approximately 26 times

higher than that of the CoS. This photocatalytic activity surpasses most of the photocatalysts as listed in Table S4. The enhanced photocatalytic performance of H_2 and CO generation result from the unique hierarchical hollow core–shell heterostructure, which is beneficial for separating and migrating photoinduced charges. After photocatalytic reaction, the peaks of CoS, ZIS, and CdS do not change, however, the (102) planes of CoS@ZIS is different from the fresh sample, the (110) diffraction plane of CoS@ZIS/CdS has decreased (Fig. S20). FTIR patterns of the used CoS, ZIS, CdS, CoS@ZIS and CoS@ZIS/CdS are lower than those of the fresh sample, but the patterns remain unchanged (Fig. S21), demonstrating that the structure of photocatalysts do not change. In Fig. 7(f), CoS@ZIS/CdS maintains high CO and H_2 generation efficiency even after five cycles, the intensities of the peaks in the XRD (Fig. S18) and FTIR (Fig. S19) patterns of the used CoS@ZIS/CdS are lower than fresh CoS@ZIS/CdS, however, XRD and FTIR spectras remain unchanged, demonstrating high stability of CoS@ZIS/CdS in the photocatalytic reaction.

3.6. Photocatalytic mechanism

Based on the results above, the possible photocatalytic charge-transfer mechanism of the CoS@ZIS/CdS heterostructure in H_2 evolution and CO_2 reduction reactions are described. In Fig. 8(a), the hollow structure promotes multiple reflections of solar light inside the cavity and fast mass transfer, accordingly achieving higher photocatalytic activity than the solid heterojunction [49]. The charge transfer at the

interfacial phase may follow the type II or Z-scheme transfer mechanism. If the type II mechanism is adopted, the reduction reaction would proceed on the CB of ZIS. Owing to the CB of ZIS (-0.32 eV) is lower than the standard potential for CO_2 reduction to CO (-0.53 V vs. NHE). So the CO can not be produced. According to above results, CO has been produced over CoS@ZIS of 69.83 μmol h^{-1} g^{-1}. Therefore, the hypothesis of the type II mechanism is invalid. Thus, the charge transfer of the CoS@ZIS/CdS takes Z-scheme under our experimental conditions. The strong interaction among CoS, ZIS, and CdS initiates the transfer of e^-. In Fig. 8(b), the CB of CoS (-0.95 V vs. NHE) and CdS (-0.61 V vs. NHE) [50] are lower than the standard potential for CO_2 reduction to CH_4 (-0.24 V vs. NHE) and CO (-0.53 V vs. NHE), hence, the CB of ZIS does not have the ability to produce CO by photocatalytic CO_2 reduction, thereby forming double Z-scheme heterojunction. Owing to the presence of a double Z-scheme heterojunction, the recombination possibility of photoexcited e^- and h^+ decreases significantly, which leads to the photoexcited e^- from CB of ZIS recombines with the existing h^+ of the VB of CoS and CdS, more reductive photoinduced e^- will store in the CB of CoS and CdS, for efficiently converting CO_2 into CO and CH_4 [51]. In addition, the CB of CoS and CdS are lower than the standard of $O_2/\cdot O_2^-$ (-0.33 V vs. NHE), therefore, the photoinduced e^- at the CB of CoS and CdS transform oxygen into$\cdot O_2^-$, to degrade BPA. Therefore, the h^+ on the VB of ZIS reacts with H_2O to produce O_2 and H^+. Furthermore, in the photocatalytic H_2 generation system, the e^- on the CB of CoS and CdS can directly react with H^+ to generate H_2. The detailed process for BPA degradation, CO_2 photoreduction and H_2 evolution on the CoS@ZIS/CdS composites are shown using the following equations:

$$CoS@ZIS/CdS + h\nu \rightarrow h^+ + e^- \tag{2}$$

$$CO_2 + 8H^+ + 8e^- \rightarrow CH_4 + 2H_2O \tag{3}$$

$$CO_2 + 2H^+ + 2e^- \rightarrow CO + H_2O \tag{4}$$

$$2H^+ + 2e^- \rightarrow H_2 \tag{5}$$

$$O_2 + e^- \rightarrow \cdot O_2^- \tag{6}$$

$$\cdot O_2^- + H^+ \rightarrow \cdot OOH \tag{7}$$

$$\cdot OOH + BPA \rightarrow CO_2 + H_2O \tag{8}$$

$$2H_2O + 4h^+ \rightarrow 4H^+ + O_2 \tag{9}$$

4. Conclusions

The hollow core–shell nanoreactor is fabricated for efficient photocatalytic CO_2 reduction and H_2 generation. The unique hollow core-shell CoS@ZIS/CdS nanoreactor generates high surface reactivity, improves carrier separation and prolongs the lifetime of photoexcited carriers, consequently, facilitates a remarkable CO_2 conversion and H_2 production efficiencies. Furthermore, the CoS@ZIS/CdS broadens the vis–NIR light absorption to generate excellent photothermal effect. Furthermore, the compatible band structures of CoS, ZIS, and CdS enable the construction the CoS@ZIS/CdS heterojunction. The work function and fermi level among three materials construct internal electric field and energy band bending at the coupling interface, facilitating a strong driving force for the construction of the CoS@ZIS/CdS. The photocatalytic mechanisms are also proposed in detail. This novel strategy presents the design and fabrication of hollow and core-shell nanoreactor as efficient heterojunction photocatalysts.

CRediT authorship contribution statement

Yan Zhang: Conceptualization, Methodology, Software, Data curation, Writing – original draft, Visualization, Investigation, Validation, Writing – review & editing. **Weihao Zhang:** Conceptualization,

Methodology, Software, Supervision, Writing – review & editing. **Yixiao Wu:** Visualization, Investigation, Software, Validation. **Liang Wan**: Visualization, Investigation. **Huijun Ding:** Supervision. **Huixiang Li:** Supervision. **Xiyang Wang:** DFT calculations.

Declaration of Competing Interest

The authors declare that they have no known competing financial interests or personal relationships that could have appeared to influence the work reported in this paper.

Acknowledgments

Appendix A. Supplementary material

Supplementary data associated with this article can be found in the online version at doi:10.1016/j.apcatb.2022.121255.

References

[1] Y. Li, S.L. Ma, S.J. Xu, H.C. Fu, Z.Q. Li, K. Li, K. Sheng, J.G. Du, X. Lu, X.H. Li, S. L. Liu, Novel magnetic biochar as an activator for peroxymonosulfate to degrade bisphenol A: emphasizing the synergistic effect between graphitized structure and CoFe$_2$O$_4$, Chem. Eng. J. 387 (2020), 124094.

[2] R.S. Sahu, Y. Shih, W.L. Chen, New insights of metal free 2D graphitic carbon nitride for photocatalytic degradation of bisphenol A, J. Hazard. Mater. 402 (2021), 123509.

[3] T. Kong, Y. Jiang, Y. Xiong, Photocatalytic CO$_2$ conversion: what can we learn from conventional COx hydrogenation, Chem. Soc. Rev. 49 (2020) 6579–6591.

[4] A.S. Hall, Y. Yoon, A. Wuttig, Y. Surendranath, Mesostructure-induced selectivity in CO$_2$ reduction catalysis, J. Am. Chem. Soc. 137 (2015) 14834–14837.

[5] W. Tu, Y. Zhou, Z. Zou, Photocatalytic conversion of CO$_2$ into renewable hydrocarbon fuels: state-of-the-art accomplishment, challenges, and prospects, Adv. Mater. 26 (2014) 4607–4626.

[6] D. Raciti, K.J. Livi, C. Wang, Highly dense Cu nanowires for low-overpotential CO$_2$ reduction, Nano Lett. 15 (2015) 6829–6835.

[7] Y. Wang, L. Cao, N.J. Libretto, X. Li, C. Li, Y. Wan, C. He, J. Lee, J. Gregg, H. Zong, D. Su, J.T. Miller, T. Mueller, C. Wang, Ensemble effect in bimetallic electrocatalysts for CO$_2$ reduction, J. Am. Chem. Soc. 141 (2019) 16635–16642.

[8] K. Li, B. Peng, T. Peng, Recent advances in heterogeneous photocatalytic CO$_2$ conversion to solar fuels, ACS Catal. 6 (2016) 7485–7527.

[9] M.J. Liu, Z.P. Xing, Z.Z. Li, W. Zhou, Recent advances in core–shell metal organic frame-based photocatalysts for solar energy conversion, Coord. Chem. Rev. 446 (2021), 214123.

[10] Y.L. Qiu, Z.P. Xing, M.J. Guo, Z.Z. Li, N. Wang, Wei Zhou, Hollow cubic Cu$_{2-x}$S/Fe-POMs/AgVO$_3$ dual Z-scheme heterojunctions with wide-spectrum response and enhanced photothermal and photocatalytic-fenton performance, Appl. Catal. B Environ. 298 (2021), 120628.

[11] M. Zhang, C.M. Xiao, X. Yan, S.S. Chen, C.H. Wang, R. Luo, J.W. Qi, X.Y. Sun, L. J. Wang, J.S. Li, Efficient removal of organic pollutants by metal−organic framework derived Co/C yolk−shell nanoreactors: size-exclusion and confinement effect, Environ. Sci. Technol. 54 (2020) 10289–10300.

[12] Y. Long, S.Y. Song, J. Li, L.L. Wu, Q.S. Wang, Y. Liu, R.C. Jin, H.J. Zhang, Pt/CeO$_2$@MOF core@shell nanoreactor for selective hydrogenation of furfural via the channel screening effect, ACS Catal. 8 (2018) 8506–8512.

[13] J. Wang, X. Luo, C. Young, J. Kim, Y.V. Kaneti, J. You, Y.M. Kang, Y. Yamauchi, K. C.W. Wu, A glucose-assisted hydrothermal reaction for directly transforming metal-organic frameworks into hollow carbonaceous materials, Chem. Mater. 30 (2018) 4401–4408.

[14] S. Zhang, D. Zhai, T. Sun, A. Han, Y. Zhai, W.C. Cheong, Y. Liu, C. Su, D. Wang, Y. Li, In situ embedding Co$_9$S$_8$ into nitrogen and sulfur codoped hollow porous carbon as a bifunctional electrocatalyst for oxygen reduction and hydrogen evolution reactions, Appl. Catal. B Environ. 254 (2019) 186–193.

[15] Y. Yang, H. Yao, Z. Yu, S.M. Islam, H. He, M. Yuan, Y. Yue, K. Xu, W. Hao, G. Sun, H. Li, S. Ma, P. Zapol, M.G. Kanatzidis, Hierarchical nanoassembly of MoS$_2$/Co$_9$S$_8$/Ni$_3$S$_2$/Ni as a highly efficient electrocatalyst for overall water splitting in a wide pH range, J. Am. Chem. Soc. 141 (2019) 10417–10430.

[16] S. Ni, H. Qu, Z. Xu, X. Zhu, H. Xing, L. Wang, J. Yu, H. Liu, C. Chen, L. Yang, Interfacial engineering of the NiSe$_2$/FeSe$_2$ p-p heterojunction for promoting oxygen evolution reaction and electrocatalytic urea oxidation, Appl. Catal. B Environ. 299 (2021), 120638.

[17] L. Xie, T. Du, J. Wang, Y. Ma, Y. Ni, Z. Liu, L. Zhang, C. Yang, J. Wang, Recent advances on heterojunction-based photocatalysts for the degradation of persistent organic pollutants, Chem. Eng. J. 426 (2021), 130617.

[18] J. Lee, H. Kim, T. Lee, W. Jang, K.H. Lee, A. Soon, Revisiting polytypism in hexagonal ternary sulfide ZnIn$_2$S$_4$ for photocatalytic hydrogen production within the Z-scheme, Chem. Mater. 31 (2019) 9148–9155.

[19] X. Dang, M. Xie, F. Dai, J. Guo, J. Liu, X. Lu, Ultrathin 2D/2D ZnIn$_2$S$_4$/g-C$_3$N$_4$ nanosheet heterojunction with atomic-level intimate interface for photocatalytic hydrogen evolution under visible light, Adv. Mater. Interfaces (2021), 2100151.

[20] S. Wang, Y. Wang, S.L. Zhang, S.Q. Zang, X.W.D. Lou, Supporting ultrathin ZnIn$_2$S$_4$ nanosheets on Co/N-doped graphitic carbon nanocages for efficient photocatalytic H$_2$ generation, Adv. Mater. 31 (2019), 1903404.

[21] L. Cheng, Q. Xiang, Y. Liao, H. Zhang, CdS-based photocatalysts, Energy Environ. Sci. 11 (2018) 1362–1391.

[22] P. Zhang, S. Wang, B.Y. Guan, X.W. Lou, Fabrication of CdS hierarchical multi-cavity hollow particles for efficient visible light CO$_2$ reduction, Energy Environ. Sci. 12 (2019) 164–168.

[23] P. Tan, Y. Liu, A. Zhu, W. Zeng, H. Cui, J. Pan, Rational design of Z-scheme system based on 3D hierarchical CdS supported 0D Co$_9$S$_8$ nanoparticles for superior photocatalytic H$_2$ generation, ACS Sustain. Chem. Eng. 6 (2018) 10385–10394.

[24] S.B. Wang, B.Y. Guan, X. Wang, X.W.D. Lou, Formation of hierarchical Co$_9$S$_8$@ZnIn$_2$S$_4$ heterostructured cages as an efficient photocatalyst for hydrogen evolution, J. Am. Chem. Soc. 140 (2018) 15145–15148.

[25] C. Dai, J.M. Lim, M. Wang, L. Hu, Y. Chen, Z. Chen, H. Chen, S.J. Bao, B. Shen, Y. Li, G. Henkelman, M. Xu, Honeycomb-like spherical cathode host constructed from hollow metallic and polar Co$_9$S$_8$ tubules for advanced lithium-sulfur batteries, Adv. Funct. Mater. 28 (2018), 1704443.

[26] Y. He, H. Rao, K. Song, J. Li, Y. Yu, Y. Lou, C. Li, Y. Han, Z. Shi, S. Feng, 3D Hierarchical ZnIn$_2$S$_4$ nanosheets with rich Zn vacancies boosting photocatalytic CO$_2$ reduction, Adv. Funct. Mater. 29 (2019), 1905153.

[27] T. Zhao, Z. Xing, Z. Xiu, Z. Li, S. Yang, W. Zhou, Oxygen-doped MoS$_2$ nanospheres/CdS quantum dots/g-C$_3$N$_4$ nanosheets super-architectures for prolonged charge lifetime and enhanced visible-light-driven photocatalytic performance, ACS Appl. Mater. Interfaces 11 (2019) 7104–7111.

[28] T.Q. Hou, Z.R. Jia, B.B. Wang, H.B. Li, X.H. Liu, L. Bi, G.L. Wu, MXene-based accordion 2D hybrid structure with Co$_9$S$_8$/C/Ti$_3$C$_2$Tx as efficient electromagnetic wave absorber, Chem. Eng. J. 414 (2021), 128875.

[29] G.C. Zuo, Y.T. Wang, W.L. Teo, A. Xie, Y. Guo, Y.X. Dai, W.Q. Zhou, D.L. Jana, Q. M. Xian, W. Dong, Y.L. Zhao, Ultrathin ZnIn$_2$S$_4$ nanosheets anchored on Ti$_3$C$_2$T$_X$ MXene for photocatalytic H$_2$ evolution, Angew. Chem. 132 (2020) 11383–11388.

[30] P.J. Chawla, S.P. Lochab, N.F. Singh, Photoluminescence, thermoluminescence and Raman studies of CdS nanocrystalline phosphor, J. Alloy. Compd. 492 (2010) 662–666.

[31] Z.F. Huang, J. Song, K. Li, M. Tahir, Y.T. Wang, L. Pan, L. Wang, X. Zhang, J.J. Zou, Hollow cobalt-based bimetallic sulfide polyhedra for efficient all-pH-value electrochemical and photocatalytic hydrogen evolution, J. Am. Chem. Soc. 138 (2016) 1359–1365.

[32] C.L. Dai, J.M. Lim, M.Q. Wang, L.Y. Hu, Y.M. Chen, Z.Y. Chen, H. Chen, S.J. Bao, B. L. Shen, Y. Li, G. Henkelman, M.W. Xu, Honeycomb-like spherical cathode host constructed from hollow metallic and polar Co$_9$S$_8$ tubules for advanced lithium–sulfur batteries, Adv. Funct. Mater. 28 (2018), 1704443.

[33] S. Wang, B.Y. Guan, X.W.D. Lou, Construction of ZnIn$_2$S$_4$-In$_2$O$_3$ hierarchical tubular heterostructures for efficient CO$_2$ photoreduction, J. Am. Chem. Soc. 140 (2018) 5037–5040.

[34] Q.M. Sun, N. Wang, J.H. Yu, J.C. Yu, A hollow porous CdS photocatalyst, Adv. Mater. 30 (2018), 1804368.

[35] M.K.Y. Chan, G. Ceder, Efficient band gap prediction for solids, Phys. Rev. Lett. 105 (2010), 196403.

[36] G.H. Zuo, Y.T. Wang, W.L. Teo, Q.M. Xian, Y.L. Zhao, Direct Z-scheme TiO$_2$–ZnIn$_2$S$_4$ photocatalyst-free photocatalytic water splitting, Appl. Catal. B Environ. 291 (2021), 120126.

[37] X. Li, K. Li, S. Zhu, K. Fan, L. Lyu, H. Yao, Y. Li, J. Hu, H. Huang, Y.W. Mai, J. B. Goodenough, Fiber-in-tube design of Co$_9$S$_8$-carbon/Co$_9$S$_8$: enabling efficient sodium storage, Angew. Chem. Int. Ed. 58 (2019) 6239–6243.

[38] G. Zhang, D. Chen, N. Li, Q. Xu, H. Li, J. He, J. Lu, Construction of hierarchical hollow Co$_9$S$_8$/ZnIn$_2$S$_4$ tubular heterostructures for highly efficient solar energy conversion and environmental remediation, Angew. Chem. Int. Ed. 59 (2020) 8255–8261.

[39] M. Wang, G. Zhang, Z. Guan, J. Yang, Q. Li, Spatially separating redox centers and photothermal effect synergistically boosting the photocatalytic hydrogen evolution of ZnIn$_2$S$_4$ nanosheets, Small (2021), 2006952.

[40] X. Wang, J. Chen, Q. Li, L. Li, Z. Zhuang, F.F. Chen, Y. Yu, Light-driven syngas production over defective ZnIn$_2$S$_4$ nanosheets, Chem 27 (2021) 3786–3792.

[41] X. Yao, X. Hu, W. Zhang, X. Gong, X. Wang, S.C. Pillai, D.D. Dionysiou, D. Wang, Mie resonance in hollow nanoshells of ternary TiO$_2$-Au-CdS and enhanced photocatalytic hydrogen evolution, Appl. Catal. B Environ. 276 (2020), 119153.

[42] Z.Z. Zhu, X.X. Li, Y.T. Qu, F.Y. Zhou, Z.Y. Wang, W.Y. Wang, C.M. Zhao, H.J. Wang, L.Q. Li, Y.G. Yao, Q. Zhang, Y. Wu, A hierarchical heterostructure of CdS QDs confined on 3D ZnIn$_2$S$_4$ with boosted charge transfer for photocatalytic CO$_2$ reduction, Nano Res. 14 (2021) 81–90.

[43] B. Qiu, Q. Zhu, M. Du, L. Fan, M. Xing, J. Zhang, Efficient solar light harvesting CdS/Co$_9$S$_8$ hollow cubes for Z-scheme photocatalytic water splitting, Angew. Chem. Int. Ed. 56 (2017) 2684–2688.

[44] W. Yang, L. Zhang, J. Xie, X. Zhang, Q. Liu, T. Yao, S. Wei, Q. Zhang, Y. Xie, Enhanced photoexcited carrier separation in oxygen-doped ZnIn$_2$S$_4$ nanosheets for hydrogen evolution, Angew. Chem. Int. Ed. 55 (2016) 6716–6720.

[45] J.X. Lv, Z.M. Zhang, J. Wang, X.L. Lu, W. Zhang, T.B. Lu, In situ synthesis of CdS/graphdiyne heterojunction for enhanced photocatalytic activity of hydrogen production, ACS Appl. Mater. Interfaces 11 (2019) 2655–2661.

[46] Z.Q. Wang, Z.Q. Yang, R.M. Fang, Y.F. Yan, J.Y. Ran, L. Zhang, A state-of-the-art review on action mechanism of photothermal catalytic reduction of CO$_2$ in full solar spectrum, Chem. Eng. J. 429 (2022), 132322.

[47] K. Wang, Z.P. Xing, D. Meng, S.Y. Zhang, Z.Z. Li, K. Pan, W. Zhou, Hollow MoSe$_2$@Bi$_2$S$_3$/CdS core-shell nanostructure as dual Z-scheme heterojunctions with enhanced full spectrum photocatalytic-photothermal performance, Appl. Catal. B Environ. 281 (2021), 119482.

[48] T.X. Zhang, F.L. Meng, Y. Cheng, N. Dewangan, G.W. Ho, S. Kawi, Z-scheme transition metal bridge of Co$_9$S$_8$/Cd/CdS tubular heterostructure for enhanced photocatalytic hydrogen evolution, Appl. Catal. B Environ. 286 (2021), 119853.

[49] B.C. Qiu, Q.H. Zhu, M.M. Du, L.G. Fan, M.Y. Xing, J.L. Zhang, Efficient solar light harvesting CdS/Co$_9$S$_8$ hollow cubes for Z-scheme photocatalytic water splitting, Angew. Chem. 129 (2017) 2728–2732.

[50] H.P. Song, A.L. Yang, H.Y. Wei, Y. Guo, B. Zhang, G.L. Zheng, S.Y. Yang, X.L. Liu, Q.S. Zhu, Z.G. Wang, T.Y. Yang, H.H. Wang, Determination of wurtzite InN/cubic In$_2$O$_3$ heterojunction band offset by x-ray photoelectron spectroscopy, Appl. Phys. Lett. 94 (2009), 222114.

[51] Y.F. Miao, R.T. Guo, J.W. Gu, Y.Z. Liu, G.L. Wu, C.P. Duan, W.G. Pan, Z-scheme Bi/Bi$_2$O$_2$CO$_3$/layered double-hydroxide nanosheet heterojunctions for photocatalytic CO$_2$ reduction under visible light, ACS Appl. Nano Mater. 4 (2021) 4902–4911.